Cell Reports
Physical Science

CellPress
OPEN ACCESS

Article

Control over cathodic deposition of continuous UiO-66 films for ion-selective transport

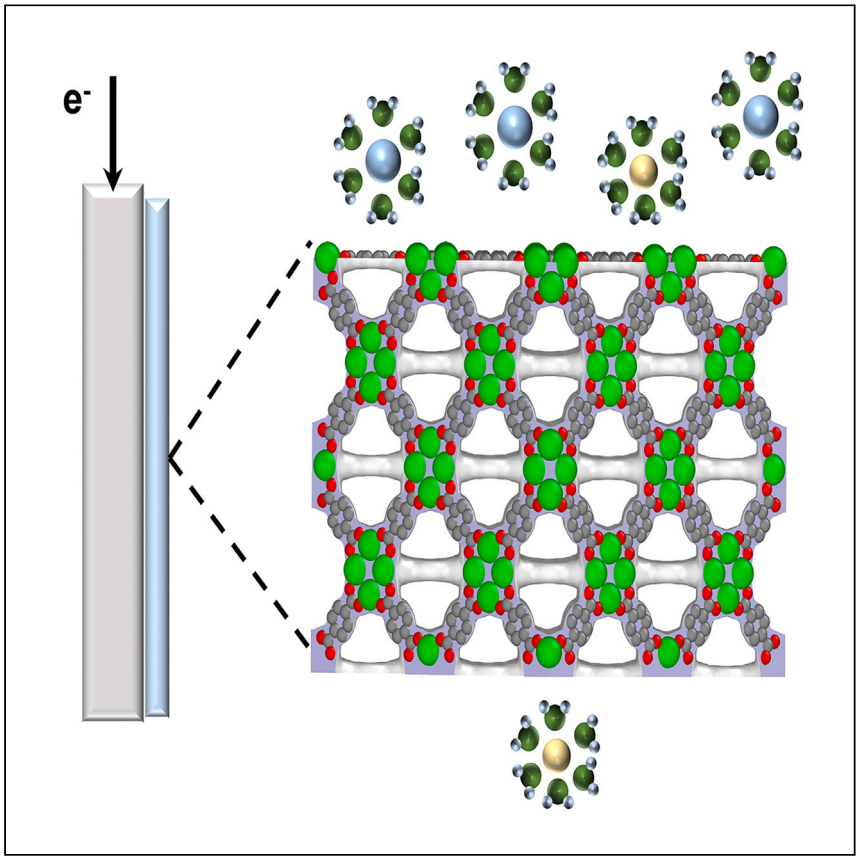

Xie et al. propose and develop a one-step cathodic deposition method for *in situ* growth of continuous UiO-66 thin films. This method is simple, convenient, and controllable, and the cathodically deposited UiO-66 membrane shows high lithium/magnesium selectivity.

Sijie Xie, Wouter Monnens, Wei Zhang, ..., Ivo F.J. Vankelecom, Xuan Zhang, Jan Fransaer

xuan.zhang@kuleuven.be

Highlights

One-step cathodic deposition of morphology-controlled UiO-66 films is designed

Cathodic deposition is fast and controllable

Deposited continuous films show excellent ion-selective transport

Xie et al., Cell Reports Physical Science 4, 101412
May 17, 2023 © 2023 The Authors.
https://doi.org/10.1016/j.xcrp.2023.101412

Cell Reports
Physical Science

CellPress
OPEN ACCESS

Article

Control over cathodic deposition of continuous UiO-66 films for ion-selective transport

Sijie Xie,[1,2] Wouter Monnens,[1] Wei Zhang,[1] Wei Guo,[1] Ning Han,[1] Zhenyu Zhou,[1] Zhenhong Xue,[1] Ivo F.J. Vankelecom,[3] Xuan Zhang,[1,2,4,*] and Jan Fransaer[1]

SUMMARY

Continuous UiO-66 films are promising for ion sieving because of their sub-nanometer-sized apertures and high chemical stability, but their preparation is challenging. Here, we report a direct cathodic deposition of UiO-66 films, which is fast, convenient, and controllable. Electrochemical measurements suggest that lithium nitrate accelerates deprotonation of carboxylic linkers and yields UiO-66 films within 1 h. Material characterizations reveal that the crystallinity of the deposited UiO-66 films improves with deposition temperature and that the morphology is controlled by the molar ratio of the ditopic linker to the monotopic modulator. Crystalline and continuous UiO-66 films are obtained with a linker-to-modulator ratio of 1:120 at 120°C. The anodic aluminum oxide membrane-supported continuous UiO-66 films display excellent selective ion transport performance with a lithium/magnesium selectivity of 286 and a lithium permeance of 11.2 mol m^{-2} h^{-1}, placing them among the best metal-organic framework (MOF) membranes reported in literature.

INTRODUCTION

Efficient ion sieving for lithium-ion extraction from brines is crucial for modern chemical engineering, especially the battery industry.[1–3] Compared with other techniques, like electrodialysis, solvent extraction, and selective adsorption, membrane technology that relies on selective discrimination of ions on the basis of their size is faster, cheaper, and cleaner.[4–6] However, most polymer membranes or mixed-matrix membranes (MMMs) suffer from poor separation performance and plasticization-induced performance degradation, which limit their large-scale application.[6–8] These issues motivate researchers to explore new materials for efficient and durable membranes.

Metal-organic frameworks (MOFs) are porous materials comprising metal nodes linked by organic ligands.[9,10] Because of their highly ordered pore structures and tunable physical/chemical properties, MOF films have garnered attention as separation media for ion sieving.[11–13] For example, Guo et al.[14] reported an HKUST-1 film-based membrane that exhibited a Li^+/Mg^{2+} selectivity of 1,815. In their subsequent work, Li^+/Mg^{2+} selectivity was improved to 4,913 by replacing HKUST-1 with ZIF-8 at the expense of Li^+ permeation, which dropped from 6.75 mol m^{-2} h^{-1} to 0.46 mol m^{-2} h^{-1}.[15] Li et al.[16] fabricated anodic aluminum oxide (AAO)-supported ZIF-90 membranes that efficiently separated Li^+ from K^+ and Na^+. Nevertheless, most of the reported HKUST-1 or ZIF series membranes are limited by their poor chemical stability in aqueous solutions (especially in acidic solutions), rendering them useless for industrial applications.[17,18]

[1]Department of Materials Engineering, KU Leuven, Kasteelpark Arenberg 44, 3001 Heverlee, Belgium

[2]ZJU-Hangzhou Global Scientific and Technological Innovation Centre, Zhejiang University, Hangzhou 311200, P.R. China

[3]Centre for Surface Chemistry and Catalysis, KU Leuven, Celestijnenlaan 200F, 3001 Leuven, Belgium

[4]Lead contact

*Correspondence: xuan.zhang@kuleuven.be

https://doi.org/10.1016/j.xcrp.2023.101412

This is an open access article under the CC BY-NC-ND license (http://creativecommons.org/licenses/by-nc-nd/4.0/).

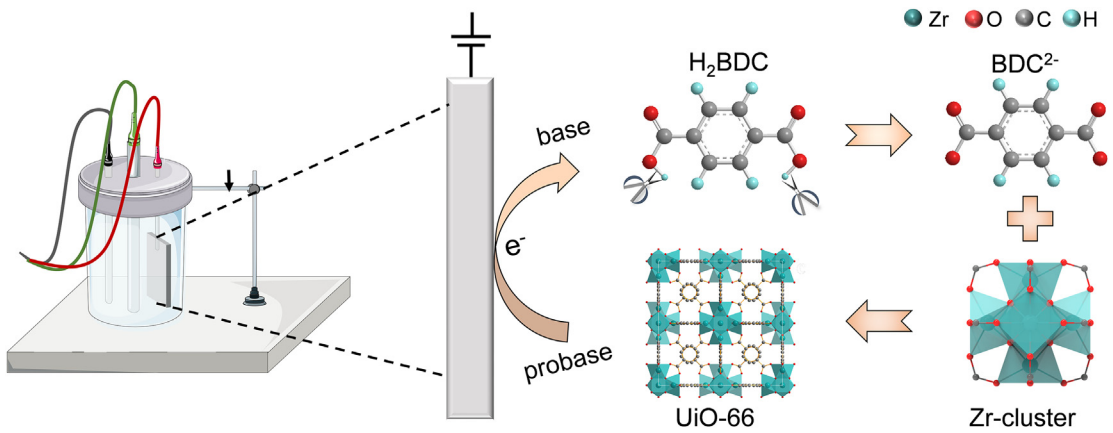

Figure 1. Schematic of nitrate-assisted cathodic deposition of UiO-66 films

A diagram depicting the electrochemical setup for probase-assisted deposition of UiO-66 is shown (atoms depicted: dark blue, Zr; red, O; gray, C; light blue, H).

UiO-66 ($Zr_6O_4(OH)_4(BDC)_6$; BDC = 1,4-benzenedicarboxy-late) is a MOF well known for its superior chemical, thermal, and mechanical stability because of its strong metal-ligand bonds and robust 12-connected Zr-based clusters.[19–21] UiO-66 contains two separate cavities (a tetrahedron cavity and an octahedron one) with rigid triangular apertures of 7.5 Å.[17] These characteristics make UiO-66 a prospective material for separations. However, synthesizing continuous crystalline UiO-66 films is challenging because of the harsh conditions required to grow UiO-66 units.[22,23] It was only in 2015 that Liu et al.[24] reported the first UiO-66 membrane.[24] They deposited a dense UiO-66 film on a hollow yttria-stabilized zirconia fiber via a solvothermal method. The composite film exhibited outstanding desalination performance. Nonetheless, the solvothermal process is energy consuming (3 days at 120°C) and sensitive to the substrate, hindering its large-scale preparation. Recently, Zhou et al.[25] reported a second approach to fabricating UiO-66 membranes using electrochemistry. In this method, linker deprotonation is initiated by the electrochemical hydrogen evolution reaction (HER). This last work opens a new door for fabrication of UiO-66 films, but several issues remain. First, the amount of protons in the deposition bath (pH ~2–3) is limited, leading to a slow deprotonation rate of the linkers, a small current density (0.26 mA cm^{-2}), and a long deposition time (>2 h).[25] Second, this method requires preparation of a Zr-based hexanuclear cluster solution (2 weeks at room temperature) via a solvothermal process ahead of the electrochemical deposition.

Given the drawbacks of the reported approaches, we present one-step nitrate-assisted cathodic deposition of UiO-66 films (Figure 1) in this work, which is fast, convenient, and controllable. Specifically, lithium nitrate was added to the deposition bath as a probase to accelerate the electrochemical deprotonation of linkers, which enables deposition of UiO-66 films in less than 1 h. The deposition temperature was raised to 120°C to improve the crystallinity of the deposited UiO-66 films. Importantly, monocarboxylic acids were used to tune the morphology of the deposits. Continuous and intergrown UiO-66 films were obtained with a linker-to-modulator molar ratio of 1:120. Continuous UiO-66 films supported on an AAO membrane display excellent ion transport with a Li^+/Mg^{2+} selectivity of 286 and permeance of 11.2 mol m^{-2} h^{-1}, which surpasses most of the reported MOF membranes. This work introduces one-step cathodic deposition of highly connected MOF films like UiO-66 films with controllable morphology, which might lead to practical applications of these MOF films in industry.

CellPress
OPEN ACCESS

RESULTS AND DISCUSSION

Selection of solvent

To achieve direct cathodic deposition of UiO-66 films without pre-preparation of Zr-based hexanuclear cluster solution, the deposition precursor should contain the metal source (e.g., $ZrCl_4$) and organic linker (H_2BDC). Hence, avoiding direct nucleation of MOF units in the deposition precursor is essential, especially at higher temperatures. In the solvothermal synthesis of UiO-66 and its analogs, DMF is often used as the solvent because the solubility of $ZrCl_4/ZrOCl_2$ and H_2BDC in DMF is high, and the decomposition products (organic amines) of DMF can deprotonate the linkers and trigger MOF generation directly.[19,26–28] However, in cathodic deposition of UiO-66 films, the deprotonation of linkers is expected to be controlled by the electrochemical reactions on the WE. Therefore, we anticipate that DMF is not the best option for direct cathodic deposition of UiO-66 films. DMSO could be a competitive alternative to DMF because its decomposition products (organic sulfides) have little influence on the deprotonation process and it has a stronger interaction with both metal ions and linkers.[29–31] A batch of deposition solutions comprising the same solutes (25 mM $ZrCl_4$, 50 mM H_2BDC, 500 mM H_2O, and 6 M acetic acid) but different solvents (0%–100% DMSO/DMF) was made to show the influence of solvent. As shown in Figure S1, the deposition precursor with a higher content of DMSO is much less likely to become cloudy (by nucleation of UiO-66 units in bulk), and the deposition precursor with 100% DMSO remains clear after 4 h at 120°C. These observations confirmed that DMSO slows down the nucleation of UiO-66 at high temperatures and allows deprotonation of linkers to be controlled by the electrochemical reactions.

Lithium nitrate-assisted deprotonation of linkers

Cathodic deposition of MOF films relies on electrochemical deprotonation of linkers.[32–35] Although Zhou et al.[25,36] reported that organic linkers could be directly deprotonated via reduction of protons in the deposition solution (reaction 1), the deprotonation rate is limited by the low concentration of the dissociated protons from the linkers. To circumvent this issue, lithium nitrate was introduced into the deposition precursor as a probase (nitrate anion). Note that $Zr(NO_3)_4$ and $ZrO(NO_3)_2$ can also act as the probase provider, but their solubility in DMSO is small (Note S1), limiting the concentration of the probase. The role of the introduced nitrate anions in the deprotonation process was examined by cyclic voltammetry (CV). The substrate was a piece of platinum-coated silicon wafer (1 cm × 2 cm). As shown in Figure 2A, the cathodic current densities in the 50 mM H_2BDC solution with or without 0.2 M $LiNO_3$ increased sharply when the potential became more negative than −0.7 V (all potentials mentioned in this text are referenced to $Ag/Ag[cryptand]^+$ unless otherwise noted; 0.0 V vs. $Ag/Ag[cryptand]^+$ equals −0.13 V vs. SHE), while the former is considerably larger than the latter. This result indicates that more H_2BDC molecules can be deprotonated in the nitrate-containing solution at a given negative potential because the direct reduction of H_2BDC (reaction 1) and the nitrate-assisted deprotonation (reaction 2) are both two-electron transfer processes.[22,29] UV-visible (UV-vis) absorption measurements confirmed the nitrate reduction to nitrite in the linker solution (Figure S2). Figure 2B shows the Nyquist plots collected in the H_2BDC solution with and without $LiNO_3$ at an applied potential of −1.8 V. It can be seen that the charge transfer resistance of the nitrate-assisted deprotonation (reaction 2) is about 4 times smaller than that of the direct reduction of the H_2BDC (reaction 1), indicating faster kinetics of the former reaction. The CVs collected on a rotating Pt disk electrode in these solutions further confirm this result, as shown in Figures S3A and S3B. It is worth noting that the current density in the $LiNO_3$-

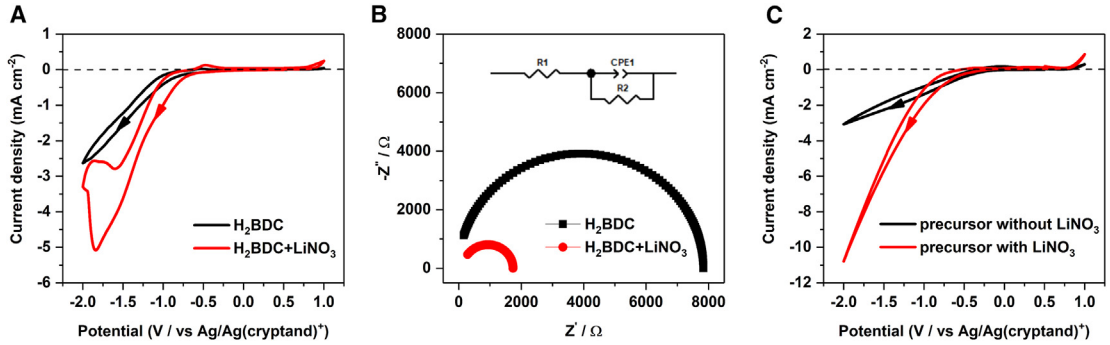

Figure 2. Electrochemical characterizations of the nitrate-containing deposition electrolyte

(A and B) CV curves (A) and Nyquist plots (B) on Pt recorded in 50 mM H_2BDC DMSO solution with or without 0.2 M $LiNO_3$; the inset shows the equivalent circuit. MTBS was used as the supporting electrolyte.

(C) CV curves on Pt recorded in 25 mM $ZrCl_4$, 50 mM H_2BDC, 500 mM H_2O, and 1 M acetic acid with and without 200 mM $LiNO_3$ DMSO solution. The scan rate for CV is 100 mV s^{-1}. The arrows shown in the CV curves represent the scan direction. The temperature was 25°C.

containing solution increases more sharply with increasing rotation speed of the electrode compared with the solution without $LiNO_3$ (also see the Levich plots in Figure S3C), even though no limiting current can be observed in either case. These results indicate that both the direct reduction of H_2BDC and the nitrate-assisted deprotonation of H_2BDC are kinetically controlled within the tested potential range, while the latter is kinetically faster. Figure 2C shows the CVs in the deposition precursor (25 mM $ZrCl_4$, 50 mM H_2BDC, 500 mM H_2O, 1 M acetic acid) with and without 200 mM $LiNO_3$. The cathodic current in the $LiNO_3$-containing precursor is nearly 4 times higher than that in the precursor without $LiNO_3$. The same trend is observed at elevated temperatures (60°C, 90°C, and 120°C), as shown in Figure S4. Based on these results, we can conclude that the use of $LiNO_3$ as a probase can significantly accelerate deprotonation of the linkers, enabling fast deposition of UiO-66 films. A similar electrochemical signal can be obtained when replacing $LiNO_3$ with $NaNO_3$ (Figure S5), indicating that the alkali cations have no influence on the deposition process:

$$H_2BDC + 2e^- \rightarrow BDC^{2-} + H_2 \quad \text{(Equation 1)}$$

$$NO_3^- + H_2BDC + 2e^- \rightarrow NO_2^- + BDC^{2-} + H_2O \quad \text{(Equation 2)}$$

Cathodic deposition of UiO-66 films at varied temperatures

Depositions at various temperatures (25°C, 60°C, 90°C, and 120°C) were conducted. The deposition precursor contained 25 mM $ZrCl_4$, 50 mM H_2BDC, 0.2 M $LiNO_3$, 500 mM H_2O, and 1 M acetic acid. After polarizing at −1.6 V for 10 min, a white film was obtained at all temperatures. The corresponding chronoamperometric curves are shown in Figure S6. It can be seen that the current density increases with deposition temperature, in line with the CVs in Figure S4. X-ray diffraction (XRD) patterns of the deposited films are shown in Figure S7. The sample prepared at room temperature (25°C) demonstrates a broad peak centered at ~8° after subtracting the signal of the substrate, suggesting its poor crystallinity. In comparison, sharp peaks of UiO-66 are observed on the XRD pattern of the sample deposited at 120°C, which indicates excellent crystallinity. Because the crystallinity of the synthesized UiO-66 is highly related to formation of $Zr_6O_4(OH)_4$ clusters,[27,28,37] it is believed that the high deposition temperature promotes *in situ* generation of Zr clusters in the deposition bath and allows direct deposition of crystalline UiO-66 films. Figure S8 shows the scanning electron microscope (SEM) images of samples

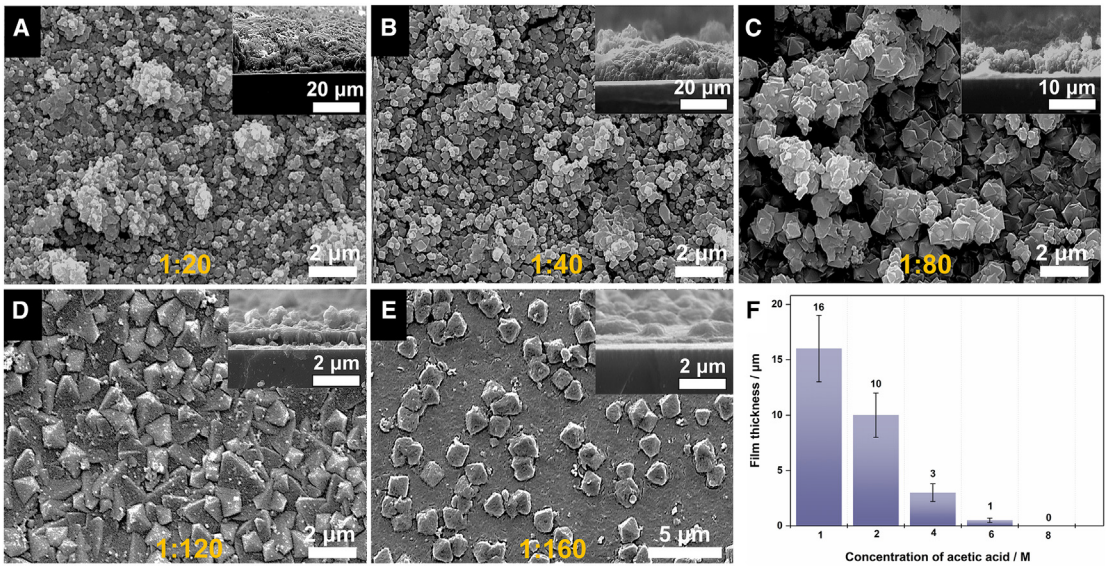

Figure 3. SEM images of the deposited UiO-66 films with a different molar ratio of H_2BDC to acetic acid

(A–E) Top-view SEM images of the UiO-66 films deposited at 120°*C* with (A) 1 M (scale bar, 2 μm), (B) 2 M (scale bar, 2 μm), (C) 4 M (scale bar, 2 μm), (D) 6 M (scale bar, 2 μm), and (E) 8 M acetic acid (scale bar, 5 μm). The gold numbers represent the H_2BDC:acetic acid molar ratio. Insets show the corresponding sectional-view SEM images. Scale bars: 20 μm (A), 20 μm (B), 10 μm (C), 2 μm (D), and 2 μm (E).

(F) Thickness of films deposited with different acetic acid concentrations.

deposited at different temperatures. All films consisting of aggregated MOF units are discontinuous and uneven. The size of the MOF crystals decreases with increasing deposition temperature, which is probably because of the improved deprotonation rate of H_2BDC at high temperatures. Interestingly, the typical octahedral crystals are hardly observed in all samples (even in the crystalline one), which might be caused by the relatively low concentration of acetic acid in the deposition precursor (see below). In addition, when $LiNO_3$ was not added to the deposition precursor, nearly no deposits were obtained with the same deposition conditions.

Cathodic deposition of UiO-66 films with varied concentrations of modulators

In the solvothermal synthesis of UiO-66, the morphology and size of UiO-66 crystals can be tuned by monotopic modulators like acetic acid.[38–40] To clarify the influence of modulators on direct cathodic deposition of UiO-66, depositions with different concentrations of monocarboxylic acid (taking acetic acid as an example) were conducted. The XRD patterns and SEM images of samples deposited at room temperature (−5 mA cm^{-2} for 1 h) with 0.25–1.5 M acetic acid are shown in Figure S9. Poorly crystalline UiO-66 films are obtained when the concentration of acetic acid is 0.5–1.0 M (H_2BDC:acetic acid molar ratio of 1:10/1:20). Nearly no deposits can be seen when the concentration reaches 1.5 M (H_2BDC:acetic acid molar ratio of 1:30). The situation changes significantly when the deposition temperature is raised to 120°C (−10 mA cm^{-2} for 1 h). As shown in Figure S10, the UiO-66 films deposited at 120°*C* are all well crystalline with an acetic acid concentration from 1–8 M (H_2BDC:acetic acid molar ratio of 1:20–1:160). Generation of an UiO-66 film with 8 M acetic acid can be attributed to the accelerated deprotonation rate at high temperatures, which ensures a decent concentration of deprotonated H_2BDC near the WE. Figure 3 shows top-view and sectional-view SEM images of these films. With increasing acetic acid concentration, the size of the deposited UiO-66 crystals grows, while the film thickness decreases (Figure 3F). Also, when acetic acid is less than 4 M, the UiO-66 films are discontinuous and comprised of small aggregated

MOF crystals (Figures 3A–3C). In contrast, only large and discrete UiO-66 crystals can be obtained when the concentration of acetic acid reaches 8 M (Figure 3E). Importantly, when the acetic acid is 6 M (i.e., the molar ratio of the linker to the modulator is 1:120), continuous, dense, and intergrown UiO-66 film can be obtained without cracks or defects (Figure 3D). The inset cross-sectional image confirms the absence of defects, showing a film adhering to the Pt substrate without delamination. XRD analysis confirmed the composition of the film to be pure UiO-66 (Figure S10). These observations suggest that the morphology of the cathodically deposited UiO-66 films can be tuned by the molar ratio of the linker to the modulator. It is worth noting that UiO-66 films with different morphologies may have different applications. For example, films with aggregated crystals can be used in catalytic applications, while continuous films are prospective separation media.[41–44]

The mechanism of this morphology tuning can be explained by the competing deprotonation of the monotopic modulator and the ditopic linker (Figure S11). Specifically, when the molar ratio of the linker to the modulator is low (i.e., the concentration of the modulator is high), deprotonation of linkers tends to be less likely, which leads to slow nucleation of UiO-66 crystals because only the deprotonated H_2BDC can link the Zr clusters. Thus, the deposited film is composed of large but discrete MOF crystals. In contrast, the low modulator content can result in fast deprotonation of H_2BDC and rapid nucleation of UiO-66 units, which causes small and aggregated UiO-66 crystals. By regulating the nucleation rate of UiO-66 crystals, a continuous UiO-66 film can be obtained.

To evaluate the flexibility of the proposed method, depositions with different monotopic modulators and ditopic linkers were conducted. First, 2-fluorobenzoic acid (pKa: 4.19 in water) and benzoic acid (pKa: 3.27 in water) were used as the modulator to replace acetic acid (pKa: 4.76 in water), respectively. It is found that the morphology of the deposited UiO-66 films remains continuous and compact using 2-fluorobenzoic acid (6 M). In comparison, it turns non-continuous when with benzoic acid (6 M) as the modulator, as shown in Figures S12A and S12B. Also, when the concentration of benzoic acid is decreased to 5 M, continuous UiO-66 films can be obtained again, as shown in Figure S12C. Because the pKa of benzoic acid is much smaller than those of the other modulators, and it is more readily deprotonated, it is unsurprising that less benzoic acid is needed for continuous UiO-66 deposition. Second, UiO-66 analogs with fumaric acid (pKa1: 3.03/pKa2: 4.4 in water) and 1,4-naphthalenedicarboxylic acid (pKa: 2.71 in water, predicted) were prepared using nitrate-assisted cathodic deposition. As shown in Figure S13, the XRD patterns of the prepared Zr-fum and Zr-naph films correspond to the simulated ones, suggesting successful MOF deposition. The top-view and cross-sectional-view SEM images of the films (Figure S13) demonstrate that both films are continuous and compact. This can be explained by the similar pKa values of fumaric acid/1,4-naphthalenedicarboxylic acid and H_2BDC (pKa1: 3.54/pKa2: 4.46 in water). According to these results, it can be deduced that the proposed cathodic deposition method is highly tolerant to the pKa changes of both modulators and organic ligands. However, the required molar ratio of the linkers to the modulators for continuous MOF films may deviate from 1:120 when using modulators/linkers different from H_2BDC/acetic acid according to the competing deprotonation theory.

Cathodic deposition of UiO-66 films on an AAO membrane

Cathodic deposition was used to fabricate AAO membrane-supported UiO-66 films, as shown schematically in Figure 4A. A Pt layer with a thickness of 25 nm was

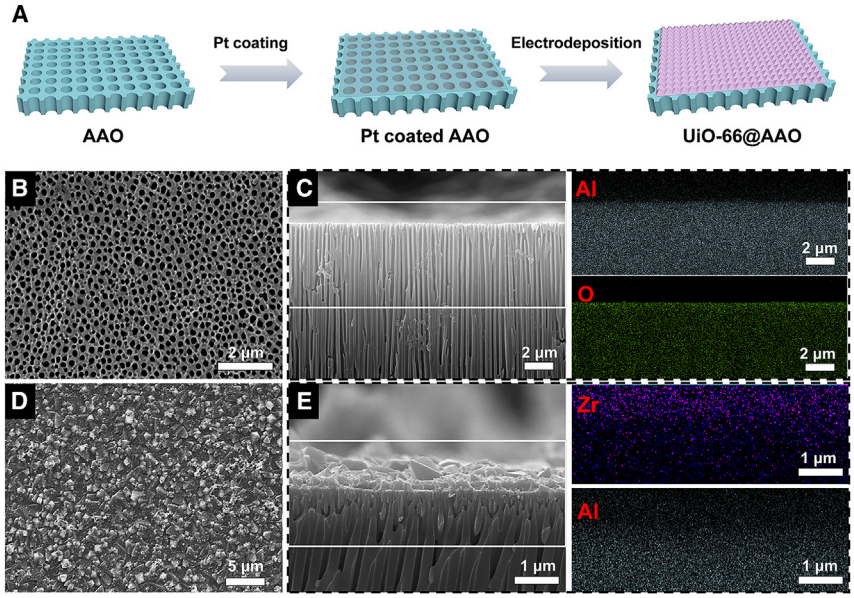

Figure 4. SEM images of a deposited UiO-66 film on an AAO membrane

(A) Schematic of preparation of the UiO-66@AAO membrane.

(B and C) Top-view SEM image of the AAO membrane (B; scale bar, 2 μm) and sectional-view SEM images of the AAO membrane (C; scale bar, 2 μm) and EDS mapping images of elements Al and O within the selected area circled by white lines.

(D and E) Top-view SEM image of the UiO-66 coated AAO membrane (D; scale bar, 5 μm) and sectional-view SEM images of the UiO-66-coated AAO membrane (E; scale bar, 1 μm) and EDS mapping images of elements Al and Zr within the selected area circled by white lines. The deposition precursor contains 25 mM $ZrCl_4$, 50 mM H_2BDC 6 M acetic acid, and 200 mM $LiNO_3$. The deposition was carried out at 120 °C with a current density of −10 mA cm^{-2} for 1 h.

pre-sputtered on top of the AAO membrane to make it electrically conductive. The top-view (Figure 4B) and sectional-view (Figure 4C) SEM images of the bare AAO membrane display uniform and parallel channels with a pore size of about 100 nm. After cathodic deposition at −10 mA cm^{-2} at 120°C for 1 h with a molar ratio of the linker to the modulator of 1:120, continuous and intergrown UiO-66 layers were deposited on the AAO substrate with a thickness of about 300 nm, as shown in the SEM images in Figures C and 4D. Notably, UiO-66 can also be seen inside the AAO channels (~40 nm thick from the surface), probably caused by the diffusion of the deprotonated linkers into these pores. XRD and Fourier transform infrared spectroscopy (FTIR) was used to characterize the UiO-66@AAO membrane. As shown in Figure S14, sharp XRD peaks of UiO-66 can be observed. Figure S15 shows the FTIR spectrum, which is similar to the reported ones, except that the commonly seen sharp peak at around 3,670 cm^{-1} (ascribing to isolated OH groups) is absent, and the broad peak centered at ~3,400 cm^{-1} is very weak.[45,46] This result is possibly due to the low concentration of intercrystalline water molecules in the deposited UiO-66 films. The calculated Brunauer-Emmett-Teller (BET) surface area of the synthesized UiO-66 film reached 864 m^2 g^{-1} according to a nitrogen adsorption test (Figure S16A), which is slightly smaller than the reported values (>1,000 m^2 g^{-1}).[47,48] The pore size distribution curve obtained from non-local density functional theory (Figure S16B) indicates that the synthesized UiO-66 contains two cavities with pore sizes of approximately 0.82 nm and 1.10 nm, respectively. This result is in line with previous reports.[49,50] According to these observations, it can be concluded that continuous and well-crystalline UiO-66 films can be coated on AAO membranes by the cathodic deposition method described in this work.

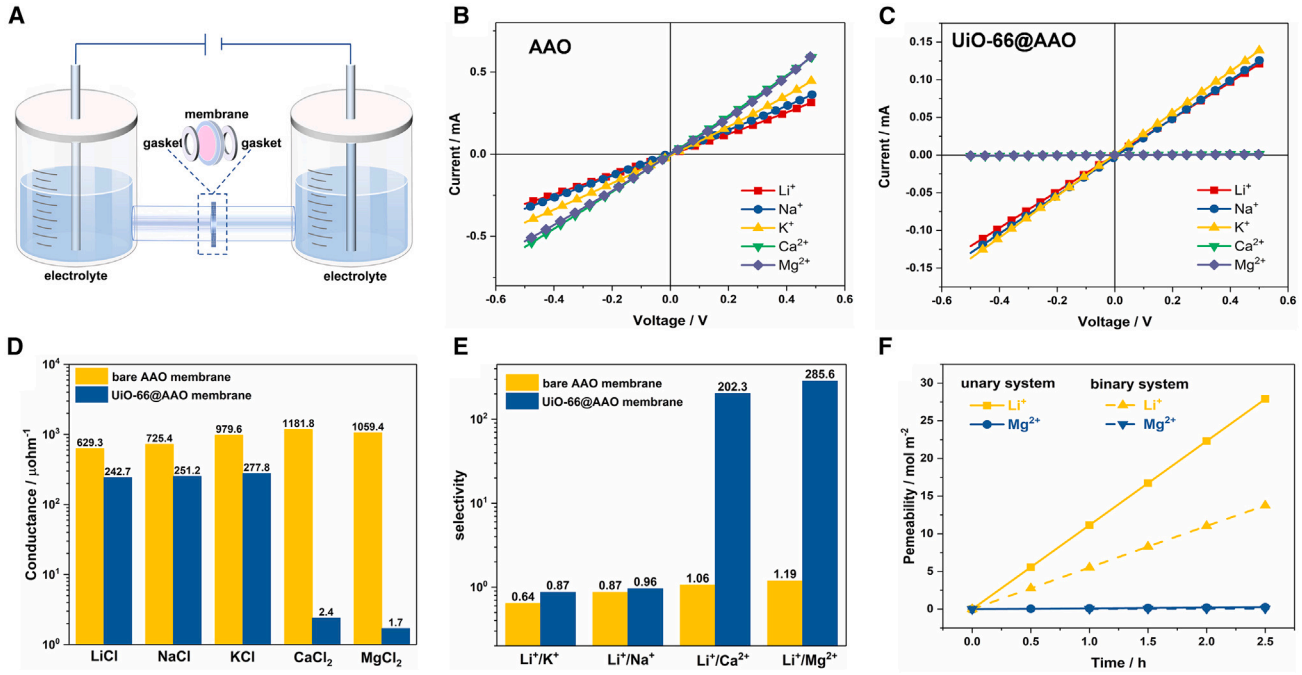

Figure 5. Selective ion transport performance of the fabricated UiO-66@AAO membrane

(A–C) Schematic of the homemade device for I-V measurements (A). Shown are I-V curves recorded in 5 different chloride solutions separated by (B) an AAO membrane or (C) an UiO-66@AAO membrane.

(D) Calculated ion conductance the of AAO and UiO-66@AAO membranes.

(E) Calculated Li^+/K^+, Li^+/Na^+, Li^+/Ca^{2+}, and Li^+/Mg^{2+} selectivity of the AAO and UiO-66@AAO membranes.

(F) Transport rates of Li^+ and Mg^{2+} across the UiO-66@AAO membrane in a unary and binary system at room temperature.

Ion-selective transport performance of the UiO-66@AAO membrane

Ion transport tests were conducted to evaluate the ion sieving performance of the deposited UiO-66@AAO membrane. As shown in Figure 5A, an H-cell-type device containing chloride solution(s) separated by a membrane was used to collect current-voltage (I-V) curves. The bare AAO membrane was tested for comparison. The I-V curves recorded in the AAO/UiO-66@AAO-separated solutions (1 M KCl, NaCl, LiCl, $CaCl_2$, and $MgCl_2$) are shown in Figures 5B and 5C, respectively. The calculated ion conductance ($G = \frac{I}{U}$; I is current, and U is the applied potential across the two electrodes) of these membranes in each solution is shown in Figure 5D. It can be seen from Figures 5B and 5C that all I-V curves are antisymmetric and go through the origin, suggesting that the surface charging of the membranes is negligible under the test conditions.[51] Importantly, the AAO membrane exhibits minor discrepancies in ion conductivity in different chloride solutions (Figure 5B). This result indicates that the bare AAO membrane cannot regulate the ion transport behavior in the tested solutions.[52] As a comparison, the I-V curves recorded in different solutions varied dramatically when using the UiO-66@AAO membrane as the separator, as shown in Figure 5C. Specifically, the ion conductivity of the UiO-66@AAO membrane in monovalent cationic solutions is over 100 times higher than those in the divalent cationic solutions. When translating the ion conductivity variations into cationic selectivity, the prepared UiO-66@AAO membrane exhibits considerable selectivity of monovalent cations to divalent cations, as shown in Figure 5E. Particularly, the Li^+/Mg^{2+} selectivity reaches 286 with a Li ion conductivity of $9.3 \times 10^{-3}\ \Omega^{-1}\ m^{-1}$. The Li^+/Mg^{2+} separation performance of the UiO-66@AAO membrane surpasses most of the previous MOF-based membranes

(Table S1), which suggests that the fabricated UiO-66@AAO membrane is a prospective separation medium for lithium extraction from Mg^{2+}/Ca^{2+}-rich lithium brines. Encouragingly, Li^+/Mg^{2+} selectivity remains nearly unchanged when the concentration of the tested $MgCl_2$ and LiCl solution changed to 0.1 M or 0.01 M, as indicated in Figure S17. Because the tested solutions contain the same chloride anions, the observed ion-selective transport across the UiO-66@AAO membrane can be attributed to the size differences of the hydrated cations ($K^+ < Na^+ < Li^+ \ll Ca^{2+} < Mg^{2+}$; Figure S18).[53] Taking the transmembrane transport of Li^+/Mg^{2+} as an example, because the dynamic window size of UiO-66 is about 7.4 Å, similar to the size of hydrated Li^+ ions (7.5 Å), and much smaller than the size of hydrated Mg^{2+} ions (8.6 Å), hydrated Li^+ ions can squeeze into the pores of UiO-66 after slight dehydration, while heavy dehydration is required for hydrated Mg^{2+}ions. Note that a rehydration process could happen when the dehydrated Li^+/Mg^{2+} has entered the octahedron cavity of UiO-66 because the size of it is about 11 Å (which is larger than the size of the hydrated Li^+/Mg^{2+}). Therefore, hydrated Li^+ and Mg^{2+} should experience multiple dehydration and rehydration processes when they pass through the UiO-66 membrane, as shown in Figure S19.

To probe the application potential of the UiO-66@AAO membranes in industrial Li production scenarios, the permeability of Li^+ and Mg^{2+} was tested by using an H-cell-type device that contains a chloride solution chamber (feed chamber) and deionized water (18.2 MΩ) chamber (Figure S20). When the feed chamber contains LiCl solution or $MgCl_2$ solution (unary ion system), the permeation of Li^+ reaches 11.2 mol m^{-2} h^{-1}, while that of Mg^{2+} is only 0.06 mol m^{-2} h^{-1} under a bias of 1 V, as shown in Figure 5F. Also, Li^+ and Mg^{2+} permeation tests at varied temperatures were conducted. As shown in Figure S20A, Li^+ and Mg^{2+} permeation increases with temperature, but the latter increases faster, resulting in a strongly decreased Li^+/Mg^{2+} selectivity of 2.7 at 70°C. This phenomenon can be explained by the larger energy barrier for Mg^{2+} permeation (20.45 kcal mol^{-1}) compared with that of Li^+ permeation (1.39 kcal mol^{-1}) (Figure S20B).[54] Because the permeability of cations across the membrane follows an Arrhenius relationship, Mg^{2+} permeation with a higher energy barrier increases faster with temperature compared with Li^+ permeation. Next, a permeation test with the feed chamber containing a mixed solution of equimolar LiCl and $MgCl_2$ (binary ion system) was conducted. The permeation of Li^+ and Mg^{2+} (5.5 mol m^{-2} h^{-1} for Li^+ and 0.04 mol m^{-2} h^{-1} for Mg^{2+}) exhibited a decrease compared with the single-ion tests, which might be caused by ion crowding in the membrane channels. However, Li^+/Mg^{2+} selectivity remains high at 187. In addition, the UiO-66 films retain their integrity and crystallinity (Figure S22) after soaking in 0.5 M LiCl-0.5 M $MgCl_2$ mixed solution for 3 months. The ionic separation performance also showed few changes (the permeation of Li^+/Mg^{2+} after 3 months was 11.2/0.06 mol m^{-2} h^{-1}, respectively).

To achieve direct cathodic deposition of UiO-66 films, several key factors should be considered. First, efficient electrochemistry-triggered deprotonation of linkers is required. Otherwise, a long deposition time is needed, or no deposit is obtained in the worst situation. Second, because the electrolyte initially contains Zr^{4+} as the metal source, generation of 12-c $Zr_6O_4(OH)_4$ metal clusters is crucial for the quality of the deposits. Third, it is well known that monocarboxylic modulators play an important role in solvothermal synthesis of UiO-66 powders by controlling the growth of UiO-66 crystals. The modulators could also be crucial for the cathodic deposition process. Given the analysis, we proposed that the addition of lithium nitrate to the electrolyte could accelerate deprotonation of linkers (H_2BDC) via the reaction of $NO_3^- + H_2BDC + 2e^- \rightarrow NO_2^- + BDC^{2-} + H_2O$. Extensive electrochemical

characterizations confirmed that deprotonation of linkers with 0.2 M lithium nitrate is 4 times faster than without lithium nitrate. Also, we found that the crystallinity of the deposited UiO-66 films improved with deposition temperature, which might be due to temperature-promoted generation of $Zr_6O_4(OH)_4$ clusters. Further, we noticed that the morphology of the deposited UiO-66 films could be tuned by the molar ratio of the linkers to the modulators via a "competing deprotonation" mechanism (the more the modulator, the slower the deprotonation of linkers). Combining these strategies allows fast deposition (less than an hour) of highly crystalline and continuous UiO-66 films, which are promising for separation applications. For example, AAO membrane-supported continuous UiO-66 films show an ion-selective transport performance with a Li^+/Mg^{2+} selectivity of 286 and a Li^+ permeance of 11.2 mol m^{-2} h^{-1}, making them some of the best MOF membranes reported in literature.

EXPERIMENTAL PROCEDURES

Resource availability

Lead contact

Further information and requests for resources and reagents should be addressed to the lead contact, Xuan Zhang (xuan.zhang@kuleuven.be).

Materials availability

This study was performed with commercially available materials and did not generate new unique reagents.

Data and code availability

Data are provided within the manuscript and supplemental information, and detailed experimental information can be found in the Supplemental experimental procedures. Requests for further information will be fulfilled by the lead contact upon request.

SUPPLEMENTAL INFORMATION

Supplemental information can be found online at https://doi.org/10.1016/j.xcrp.2023.101412.

ACKNOWLEDGMENTS

This project received funding from the FWO and F.R.S.-FNRS under the Excellence of Science (EOS) program-ECOBAT (40007515) and the National Natural Science Foundation of China (22005250). S.X., Z.Z., Z.X., W.Z., and W.G. gratefully acknowledge the China Scholarship Council. W.M. thanks the Research Foundation Flanders (FWO) for a PhD grant (1SB8319N). The authors thank Iris Cuppens for assistance with the ICP measurements, Omar Martinez Mora for help with the UV-vis tests, and Prof. Philippe Vereecken for enlightening discussions and the generous supply of Pt wafers.

AUTHOR CONTRIBUTIONS

X.Z. and J.F. supervised the project, provided financial support, and revised the manuscript. S.X. conceived the idea, designed the research, conducted the experiments, and wrote the initial manuscript. W.M. conducted part of the deposition experiments and analyzed the experimental data. W.Z., W.G., N.H., Z.Z., and Z.X. characterized some film samples and analyzed the data. I.F.J.V. provided instruments for the material characterizations and revised the manuscript.

CellPress
OPEN ACCESS

DECLARATION OF INTERESTS

The authors declare no competing interests.

Received: February 16, 2023
Revised: April 5, 2023
Accepted: April 17, 2023
Published: May 8, 2023

REFERENCES

1. Tabelin, C.B., Dallas, J., Casanova, S., Pelech, T., Bournival, G., Saydam, S., and Canbulat, I. (2021). Towards a low-carbon society: a review of lithium resource availability, challenges and innovations in mining, extraction and recycling, and future perspectives. Miner. Eng. *163*, 106743.

2. Kazemzadeh, H., Karimi-Sabet, J., Towfighi Darian, J., and Adhami, A. (2020). Evaluation of polymer inclusion membrane efficiency in selective separation of lithium ion from aqueous solution. Sep. Purif. Technol. *251*, 117298.

3. Liu, G., Zhao, Z., and Ghahreman, A. (2019). Novel approaches for lithium extraction from salt-lake brines: a review. Hydrometallurgy *187*, 81–100.

4. Chen, J.P., Mou, H., Wang, L.K., Matsuura, T., and Wei, Y. (2011). Membrane separation: basics and applications. In Membrane and desalination technologies (Springer), pp. 271–332.

5. Yang, L., Qian, S., Wang, X., Cui, X., Chen, B., and Xing, H. (2020). Energy-efficient separation alternatives: metal–organic frameworks and membranes for hydrocarbon separation. Chem. Soc. Rev. *49*, 5359–5406.

6. Qian, Q., Asinger, P.A., Lee, M.J., Han, G., Mizrahi Rodriguez, K., Lin, S., Benedetti, F.M., Wu, A.X., Chi, W.S., and Smith, Z.P. (2020). MOF-based membranes for gas separations. Chem. Rev. *120*, 8161–8266.

7. Yampolskii, Y. (2012). Polymeric gas separation membranes. Macromolecules *45*, 3298–3311.

8. Liu, Y., Xie, W., Liang, S., Li, X., Fan, Y., and Luo, S. (2022). Polyimide/ZIFs mixed matrix membranes with tunable interfacial interaction for efficient gas separation. J. Membr. Sci. *646*, 120240.

9. Jiang, H., Alezi, D., and Eddaoudi, M. (2021). A reticular chemistry guide for the design of periodic solids. Nat. Rev. Mater. *6*, 466–487. https://doi.org/10.1038/s41578-021-00287-y.

10. Zhou, H.-C., Long, J.R., and Yaghi, O.M. (2012). Introduction to metal–organic frameworks. Chem. Rev. *112*, 673–674.

11. Yang, F., Du, M., Yin, K., Qiu, Z., Zhao, J., Liu, C., Zhang, G., Gao, Y., and Pang, H. (2022). Applications of metal-organic frameworks in water treatment: a review. Small *18*, 2105715.

12. Li, W., Liu, Y.-Y., Bai, Y., Wang, J., and Pang, H. (2020). Anchoring ZIF-67 particles on amidoximerized polyacrylonitrile fibers for radionuclide sequestration in wastewater and seawater. J. Hazard Mater. *395*, 122692.

13. Zhang, W., Harty, B., Zheng, Y., Zhang, Z., Li, X., Wang, D., and Kohane, D.S. (2021). Metal-organic frameworks for C6–C8 hydrocarbon separations. EnergyChem *6*, 100057.

14. Guo, Y., Ying, Y., Mao, Y., Peng, X., and Chen, B. (2016). Polystyrene sulfonate threaded through a metal–organic framework membrane for fast and selective lithium-ion separation. Angew. Chem. *55*, 15120–15124.

15. Liang, H.-Q., Guo, Y., Peng, X., and Chen, B. (2020). Light-gated cation-selective transport in metal–organic framework membranes. J. Mater. Chem. A Mater. *8*, 11399–11405.

16. Li, R., Lu, B., Xie, Z., and Zhai, J. (2019). The confinement effect of angstrom-sized pores in asymmetrical membrane constructed by zeolitic imidazolate frameworks: partially dehydrated ion transport performance. Small *15*, 1904866.

17. Yuan, S., Feng, L., Wang, K., Pang, J., Bosch, M., Lollar, C., Sun, Y., Qin, J., Yang, X., Zhang, P., et al. (2018). Stable metal-organic frameworks: design, synthesis, and applications. Adv. Mater. *30*, 1704303.

18. Ding, M., Cai, X., and Jiang, H.L. (2019). Improving MOF stability: approaches and applications. Chem. Sci. *10*, 10209–10230. https://doi.org/10.1039/c9sc03916c.

19. Chen, Z., Hanna, S.L., Redfern, L.R., Alezi, D., Islamoglu, T., and Farha, O.K. (2019). Reticular chemistry in the rational synthesis of functional zirconium cluster-based MOFs. Coord. Chem. Rev. *386*, 32–49.

20. Cavka, J.H., Jakobsen, S., Olsbye, U., Guillou, N., Lamberti, C., Bordiga, S., and Lillerud, K.P. (2008). A new zirconium inorganic building brick forming metal organic frameworks with exceptional stability. J. Am. Chem. Soc. *130*, 13850–13851.

21. Kandiah, M., Nilsen, M.H., Usseglio, S., Jakobsen, S., Olsbye, U., Tilset, M., Larabi, C., Quadrelli, E.A., Bonino, F., and Lillerud, K.P. (2010). Synthesis and stability of tagged UiO-66 Zr-MOFs. Chem. Mater. *22*, 6632–6640.

22. Liu, X. (2020). Metal-organic framework UiO-66 membranes. Front. Chem. Sci. Eng. *14*, 216–232.

23. Stassen, I., Styles, M., Van Assche, T., Campagnol, N., Fransaer, J., Denayer, J., Tan, J.-C., Falcaro, P., De Vos, D., and Ameloot, R. (2015). Electrochemical film deposition of the zirconium metal–organic framework UiO-66 and application in a miniaturized sorbent trap. Chem. Mater. *27*, 1801–1807.

24. Liu, X., Demir, N.K., Wu, Z., and Li, K. (2015). Highly water-stable zirconium metal–organic framework UiO-66 membranes supported on alumina hollow fibers for desalination. J. Am. Chem. Soc. *137*, 6999–7002.

25. Zhou, S., Shekhah, O., Jia, J., Czaban-Jóźwiak, J., Bhatt, P.M., Ramírez, A., Gascon, J., and Eddaoudi, M. (2021). Electrochemical synthesis of continuous metal–organic framework membranes for separation of hydrocarbons. Nat. Energy *6*, 882–891. https://doi.org/10.1038/s41560-021-00881-y.

26. Chen, Y., Zhang, X., Mian, M.R., Son, F.A., Zhang, K., Cao, R., Chen, Z., Lee, S.J., Idrees, K.B., Goetjen, T.A., et al. (2020). Structural diversity of zirconium metal-organic frameworks and effect on adsorption of toxic chemicals. J. Am. Chem. Soc. *142*, 21428–21438. https://doi.org/10.1021/jacs.0c10400.

27. Valenzano, L., Civalleri, B., Chavan, S., Bordiga, S., Nilsen, M.H., Jakobsen, S., Lillerud, K.P., and Lamberti, C. (2011). Disclosing the complex structure of UiO-66 metal organic framework: a synergic combination of experiment and theory. Chem. Mater. *23*, 1700–1718.

28. Taddei, M., van Bokhoven, J.A., and Ranocchiari, M. (2020). Influence of water in the synthesis of the zirconium-based metal–organic framework UiO-66: isolation and reactivity of $[ZrCl(OH)_2(DMF)_2]Cl$. Inorg. Chem. *59*, 7860–7868.

29. Atzori, C., Shearer, G.C., Maschio, L., Civalleri, B., Bonino, F., Lamberti, C., Svelle, S., Lillerud, K.P., and Bordiga, S. (2017). Effect of benzoic acid as a modulator in the structure of UiO-66: an experimental and computational study. J. Phys. Chem. C *121*, 9312–9324.

30. Xiao, Y., Wu, Z., Zhang, Q., Li, P., Yu, H., and Lu, G. (2020). Oxygen-assisted cathodic deposition of copper-carboxylate metal-organic framework films. Cryst. Growth Des. *20*, 3997–4004.

31. Ameloot, R., Gobechiya, E., Uji-i, H., Martens, J.A., Hofkens, J., Alaerts, L., Sels, B.F., and De Vos, D.E. (2010). Direct patterning of oriented metal–organic framework crystals via control over crystallization kinetics in clear precursor solutions. Adv. Mater. *22*, 2685–2688.

32. Li, M., and Dincă, M. (2011). Reductive electrosynthesis of crystalline metal–organic frameworks. J. Am. Chem. Soc. *133*, 12926–12929.

33. Li, M., and Dincă, M. (2014). Selective formation of biphasic thin films of metal–organic frameworks by potential-controlled cathodic electrodeposition. Chem. Sci. *5*, 107–111.

34. Li, M., and Dincă, M. (2015). On the mechanism of MOF-5 formation under cathodic bias. Chem. Mater. *27*, 3203–3206.

35. Xie, S., Monnens, W., Wan, K., Zhang, W., Guo, W., Xu, M., Vankelecom, I.F.J., Zhang, X., and Fransaer, J. (2021). Cathodic electrodeposition of MOF films using hydrogen peroxide. Angew. Chem. Int. Ed. Engl. *60*, 24950–24957. https://doi.org/10.1002/anie.202108485.

36. Zhou, S., Wei, Y., Li, L., Duan, Y., Hou, Q., Zhang, L., Ding, L.-X., Xue, J., Wang, H., and Caro, J. (2018). Paralyzed membrane: current-driven synthesis of a metal-organic framework with sharpened propene/propane separation. Sci. Adv. *4*, eaau1393.

37. Xu, H., Sommer, S., Broge, N.L.N., Gao, J., and Iversen, B.B. (2019). The chemistry of nucleation: in situ pair distribution function analysis of secondary building units during UiO-66 MOF formation. Chemistry *25*, 2051–2058.

38. Vermoortele, F., Bueken, B., Le Bars, G., Van de Voorde, B., Vandichel, M., Houthoofd, K., Vimont, A., Daturi, M., Waroquier, M., Van Speybroeck, V., et al. (2013). Synthesis modulation as a tool to increase the catalytic activity of metal–organic frameworks: the unique case of UiO-66 (Zr). J. Am. Chem. Soc. *135*, 11465–11468.

39. Wißmann, G., Schaate, A., Lilienthal, S., Bremer, I., Schneider, A.M., and Behrens, P. (2012). Modulated synthesis of Zr-fumarate MOF. Microporous Mesoporous Mater. *152*, 64–70.

40. Schaate, A., Roy, P., Godt, A., Lippke, J., Waltz, F., Wiebcke, M., and Behrens, P. (2011). Modulated synthesis of Zr-based metal–organic frameworks: from nano to single crystals. Chemistry *17*, 6643–6651.

41. Bi, F., Zhao, Z., Yang, Y., Gao, W., Liu, N., Huang, Y., and Zhang, X. (2022). Chlorine-coordinated Pd single atom enhanced the chlorine resistance for volatile organic compound degradation: mechanism study. Environ. Sci. Technol. *56*, 17321–17330.

42. Chen, J., Yang, Y., Zhao, S., Bi, F., Song, L., Liu, N., Xu, J., Wang, Y., and Zhang, X. (2022). Stable black phosphorus encapsulation in porous mesh-like UiO-66 promoted charge transfer for photocatalytic oxidation of toluene and o-dichlorobenzene: performance, degradation pathway, and mechanism. ACS Catal. *12*, 8069–8081.

43. Zhang, X., Bi, F., Zhao, Z., Yang, Y., Li, Y., Song, L., Liu, N., Xu, J., and Cui, L. (2022). Boosting toluene oxidation by the regulation of Pd species on UiO-66: synergistic effect of Pd species. J. Catal. *413*, 59–75.

44. Bi, F., Zhao, Z., Yang, Y., Liu, Q., Huang, W., Huang, Y., and Zhang, X. (2022). Efficient degradation of toluene over ultra-low Pd supported on UiO-66 and its functional materials: reaction mechanism, water-resistance, and influence of SO_2. Environmental Functional Materials *1*, 166–181.

45. Atzori, C., Lomachenko, K.A., Jacobsen, J., Stock, N., Damin, A., Bonino, F., and Bordiga, S. (2020). Bimetallic hexanuclear clusters in Ce/Zr-UiO-66 MOFs: in situ FTIR spectroscopy and modelling insights. Dalton Trans. *49*, 5794–5797.

46. Tan, K., Pandey, H., Wang, H., Velasco, E., Wang, K.-Y., Zhou, H.-C., Li, J., and Thonhauser, T. (2021). Defect termination in the UiO-66 family of metal–organic frameworks: the role of water and modulator. J. Am. Chem. Soc. *143*, 6328–6332.

47. Ghosh, P., Colón, Y.J., and Snurr, R.Q. (2014). Water adsorption in UiO-66: the importance of defects. Chem. Commun. *50*, 11329–11331.

48. Garibay, S.J., and Cohen, S.M. (2010). Isoreticular synthesis and modification of frameworks with the UiO-66 topology. Chem. Commun. *46*, 7700–7702.

49. Hao, L., Li, X., Hurlock, M.J., Tu, X., and Zhang, Q. (2018). Hierarchically porous UiO-66: facile synthesis, characterization and application. Chem. Commun. *54*, 11817–11820.

50. Cao, Y., Zhao, Y., Lv, Z., Song, F., and Zhong, Q. (2015). Preparation and enhanced CO2 adsorption capacity of UiO-66/graphene oxide composites. J. Ind. Eng. Chem. *27*, 102–107.

51. Li, X., Zhang, H., Hou, J., Ou, R., Zhu, Y., Zhao, C., Qian, T., Easton, C.D., Selomulya, C., Hill, M.R., and Wang, H. (2020). Sulfonated sub-1-nm metal–organic framework channels with ultrahigh proton selectivity. J. Am. Chem. Soc. *142*, 9827–9833.

52. Zhang, H., Hou, J., Hu, Y., Wang, P., Ou, R., Jiang, L., Liu, J.Z., Freeman, B.D., Hill, A.J., and Wang, H. (2018). Ultrafast selective transport of alkali metal ions in metal organic frameworks with subnanometer pores. Sci. Adv. *4*, eaaq0066. https://doi.org/10.1126/sciadv.aaq0066.

53. Xu, R., Kang, Y., Zhang, W., Zhang, X., and Pan, B. (2022). Oriented UiO-67 metal–organic framework membrane with fast and selective lithium-ion transport. Angew. Chem. Int. Ed. Engl. *61*, e202115443.

54. Zhou, X., Wang, Z., Epsztein, R., Zhan, C., Li, W., Fortner, J.D., Pham, T.A., Kim, J.-H., and Elimelech, M. (2020). Intrapore energy barriers govern ion transport and selectivity of desalination membranes. Sci. Adv. *6*, eabd9045.